

Durable, highly sensitive conductive elastomeric nanocomposite films containing various graphene nanoplatelets and their derivatives

Qingshi Meng, Daiqiang Liu, Yi zhou, Rui Cai, Yuanyuan Feng, Zonghao Hu, and Sensen Han

Author post-print (accepted) deposited by Coventry University's Repository

Original citation & hyperlink:

Meng, Q, Liu, D, Zhou, Y & Cai, R 2023, 'Durable, highly sensitive conductive elastomeric nanocomposite films containing various graphene nanoplatelets and their derivatives', *Polymers for Advanced Technologies*, vol. 34, no. 4, pp. 1170-1181. <https://doi.org/10.1002/pat.5960>

DOI 10.1002/pat.5960

ISSN 1042-7147

ESSN 1099-1581

Publisher: Wiley

This is the peer reviewed version of the following article: Meng, Q, Liu, D, Zhou, Y & Cai, R 2023, 'Durable, highly sensitive conductive elastomeric nanocomposite films containing various graphene nanoplatelets and their derivatives', *Polymers for Advanced Technologies*, vol. 34, no. 4, pp. 1170-1181.

<https://doi.org/10.1002/pat.5960>, which has been published in final form at <https://doi.org/10.1002/pat.5960>. This article may be used for non-commercial purposes in accordance with Wiley Terms and Conditions for Use of Self-Archived Versions. This article may not be enhanced, enriched or otherwise transformed into a derivative work, without express permission from Wiley or by statutory rights under applicable legislation. Copyright notices must not be removed, obscured or modified. The article must be linked to Wiley's version of record on Wiley Online Library and any embedding, framing or otherwise making available the article or pages thereof by third parties from platforms, services and websites other than Wiley Online Library must be prohibited.

This document is the author's post-print version, incorporating any revisions agreed during the peer-review process. Some differences between the published version and this version may remain and you are advised to consult the published version if you wish to cite from it.

Durable, highly sensitive conductive elastomeric nanocomposite films containing various graphene nanoplatelets and their derivatives

Qingshi Meng^{a,b}, Daiqiang Liu^a, Yi Zhou^d, Rui Cai^c, Yuanyuan Feng^a, Zonghao Hu^b, Sensen Han^e

^a College of Aerospace Engineering, Shenyang Aerospace University, Shenyang 110136, China

^b Shenyang Aircraft Design Institute, AVIC, Shenyang 110135, China

^c School of Mechanical, Aerospace and Automotive Engineering, Coventry University, Coventry CV1 2JH, United Kingdom

^d Dyson School of Design Engineering, Imperial College London, London SW7 2DB, UK

^e Shi-changxu Innovation Center for Advanced Materials, Institute of Metal Research, Chinese Academy of Sciences, Shenyang 110016, China

Corresponding Author: Qingshi Meng and Sensen Han

Abstract

In recent years, the use of nano-fillers in flexible polymer matrix to prepare highly flexible, stretchable, and multifunctional product has been widely studied. However, the uneven dispersion of nano-fillers in polymer matrix is an important factor hindering their performance. In this study, a method to prepare graphene nanosheets by ball milling and modification with the silane coupling agent APTES is reported, and this method can reduce the thickness of the nanosheets, improving the dispersion effect and compatibility of the nanosheets in the PDMS matrix. The mechanical and conductive properties of the prepared composite films were further analyzed. The morphology showed that our modified graphene (MGE and BMGE) are more evenly dispersed in the PDMS matrix compared to the unmodified graphene (GNP). The MGE/PDMS composite film has significantly improved electrical conductivity. It has a wide sensing range (up to 48%), high sensitivity (GF of 152 in the 20-40% strain range) and reliable cycle repeatability (>10,000 cycles) with a response time of 0.12 s. The results show that the modified graphene/PDMS conductive elastic nanocomposite film is an ideal material for making flexible electronic products.

Key words: *graphene; PDMS; nanocomposite film; ball milling; APTES.*

1. Introduction

Highly flexible and stretchable composite films can be an important component of flexible strain sensors. Flexible strain sensors are able to respond to external mechanical deformation and converting it into electrical signals¹⁻³ while offering many advantages such as high flexibility, light weight, longevity and good compatibility.⁴⁻⁷ It has various applications such as human motion monitoring, structural monitoring, biomedicine, human-machine interaction and intelligent robotics.⁸⁻¹⁰ The sensing performance indicators commonly used to evaluate flexible strain sensors including sensitivity, linearity, sensing range, response time and repeatability, of which the most important indicator is sensitivity.^{11,12}

Nowadays, the research on flexible strain sensors is developing very rapidly. Chen et al.¹³ prepared PDMS/multi-walled carbon nanotubes (CNT)/aligned nickel particles (Ni) composites under low magnetic field conditions. The PDMS/CNT/Ni composite has significant conductive, mechanical and piezoresistive anisotropy due to the arrangement of nickel particles. Anisotropic strain sensors with different resistance trends in different directions were realized. Cai et al.¹⁴ prepared multifunctional PDMS/thermo-expandable microspheres (EM)/CNT foam elastic composites by introducing EM into PDMS/CNT. The foam elastic composite has good mechanical properties, high voltage resistance sensitivity, temperature sensitivity and electromagnetic interference shielding properties. In addition, the self-reinforced PDMS/EM/CNT elastomer has a unique softening behavior. Blending conductive nanomaterials with flexible substrate materials is a common method for preparing flexible composite films.^{15,16} However, the performance of composite films prepared using such method are often

undesirable due to the dispersion effect of the conductive nanomaterials in the flexible substrate material.¹⁷ Therefore, improving the dispersion of conductive nanomaterials in flexible substrate materials is one of the most critical problems need to be addressed during the preparation process. Yang et al.¹⁸ constructed cation- π interactions at the graphite interface to improve the delamination and dispersion of graphite in starch, and prepared graphite/starch composite coatings with significantly enhanced electrical conductivity and electromagnetic shielding effects. Wu et al.¹⁹ prepared GNPs reinforced Cu/Ti₃SiC₂/C nanocomposites by high-pressure torsion (HPT) after powder metallurgy, and the dispersion of GNPs in the matrix was significantly improved with good bonding after HPT. The mechanical and electrical properties of the nanocomposites are improved. Graphene is one of the most ideal nano-fillers for the preparation of composite films, which is due to its large surface area, excellent conductivity and stability.^{20,21} In order to solve the problem of graphene dispersion in polymer matrix, researchers have developed a variety of methods to modify graphene which two of the main methods are graphene covalent and non-covalent bond functionalization modifications.^{22,23} Covalent bond functionalization modification opens the graphene conjugate structure by grafting modification using reactive oxygen-containing functional groups on the surface of graphene.^{24,25} The main non-covalent bonding functionalized modified graphene structures are π - π bonding interactions, hydrogen bonding and ionic bonding.^{26,27} During the ball milling process, large number of oxygen-containing functional groups such as hydroxyl and carboxyl groups are grafted on the surface of graphene, which lays the chemical foundation for the modification of graphene.^{28,29} The properties of graphene-based composites can be enhanced by modifying graphene to access active groups on the graphene surface, increasing the graphene sheet spacing and improving the interfacial interaction between graphene and the polymer matrix which

enables graphene to be uniformly dispersed in the polymer matrix.³⁰⁻³²

Silane coupling agent 3-aminopropyltriethoxysilane (APTES) is an amino-end-groups containing organosilicon compound that can be used to modify graphene and improve the compatibility of graphene with polymeric substrates. The alkoxy group on APTES can react with the hydroxyl group on the graphene, and then the silane molecular functional group generates a chemical bond between graphene and the polymer matrix.³³⁻³⁵ Wang et al.³⁶ modified graphene using APTES, and they found that functionalization of graphene with silane reagents enhanced the interfacial interaction between graphene and epoxy matrix, improving the dispersion of graphene in the epoxy matrix. The tensile strength, breaking elongation and thermal stability of the composites were improved significantly. S. Woraphutthaporn et al.³⁷ modified graphene oxide using APTES and 3-(2-aminoethyl amino)propyl trimethoxysilane. The use of silane-MGO enhanced the curing time, crosslink density, and filler-rubber interaction while also improving filler dispersion, and mechanical and electrical properties of the natural rubber nanocomposites. M. Lotfi et al.³⁸ synthesized graphene oxide nanosheets and then surface-treated graphene oxide with APTES and hyperbranched polyester amide (HBP), aiming to improve epoxy resin mechanical properties especially toughness. They found that modified nanoparticles can significantly improve hardness and toughness of epoxy, the highest enhancement (2.6 times in toughness and 2.28 times in micro-hardness) was achieved with 1 wt% graphene oxide sequentially treated with APTES and HBP. Their structural studies revealed that such promotion was attributed to the simultaneous enhancement in both physical (filler dispersion) and chemical (crosslink density) aspects of the resulting network. However, there is little literature on the effects of silane coupling agents on the electrical and mechanical properties of graphene/PDMS composites. Three kinds of graphene fillers were prepared using different raw materials and processing methods.

The morphology and thickness of these three kinds of graphene fillers and their dispersion in the PDMS matrix were compared. The thermally expanded graphite intercalation compounds and ethanol were ball milled, which not only reduced the thickness of the graphene sheet but also grafted hydroxyl groups on the graphene surface. The dispersion of graphene in the PDMS matrix was improved by ball milling and APTES modification. Combining with mechanical co-blending method, three kinds of graphene/PDMS composite films were fabricated for further examination. The morphology, mechanical properties and sensing properties of the three graphene/PDMS composite films were examined. The improved dispersion of graphene in PDMS enhanced the mechanical and sensing properties of the composite films.

2. Experimental sections

2.1. Materials

Graphite intercalation compounds (GICs) and graphite powders were ordered from Qingdao Huatai Technology Co., Ltd, Shandong, China. Polydimethylsiloxane (PDMS) was supplied by Dow Corning, Jiangsu, China. Silane coupling agent 3-aminopropyltriethoxysilane (APTES) was provided by Nanjing Xuanhao New Material Technology Co., Ltd (China). *n*-Hexane was purchased from Tianjin Aopusheng Chemical Co., Ltd (China).

2.2. Fabrication of graphene conductive fillers

The fabrication method of graphene nanoplatelets (GNPs) is based on the reported studies.³⁹ Firstly, the GICs were heated using a muffle furnace, 2g GICs were placed in a crucible, and then heated in the muffle furnace at 710 °C for 1 minute to obtain the expanded GICs, 4 g of the expanded GICs were taken and mixed with acetone solution, and sonicated in an ultrasonic machine for 15 hours. Finally, the mixture was put into an electric thermostatic drying oven at 50 °C to obtain GNPs.

1 g of expanded GICs, 50 ml of ethanol and zirconia balls were put into a ball mill jar and ball milled for 15 h at 500 r/min, removed and filtered by extraction and dried at 60 °C to obtain ball-milled graphene (BGE-15 h). Then 20 g of APTES, 120 ml of deionized water and 60 ml of ethanol were added in a beaker to sonicate for 30 min to make the APTES pre-hydrolyzed. 2 g of BGE-15 h was further added and sonicated for 10 min to disperse it in the mixed solution. Finally, the mixture was water-bathing at 70 °C for 8 h, removed and washed with ethanol, dried by using an electric thermostatic drying oven at 50 °C to obtain the modified graphene (MGE).

Graphite powder is the main material for the preparation of ball-milled modified graphene (BMGE).

Firstly, 1 g of graphite powder, 50 ml of ethanol and zirconium oxide balls were put into a ball mill jar and ball milled for 9 hours at 500 r/min, removed and filtered by extraction and dried at 60 °C to obtain ball-milled graphene (BGE-9 h). Then 1 g of APTES, 10 ml of deionized water and 5 ml of ethanol were added to the beaker, sonicated for 30 min and further poured into the ball mill jar. Finally, 1 g of BGE-9 h, 35 ml of deionized water and zirconium oxide balls were added, ball milled for 3 h at 500 r/min, removed and washed with ethanol, dried at 50 °C to obtain BMGE.

2.3. Fabrication of composite films

The fabrication process of GNP/PDMS, MGE/PDMS and BMGE/PDMS composite films is shown in Figure 1. Firstly, 20 g of PDMS and the corresponding volume fraction of filler were added to a beaker and diluted with a small amount of *n*-hexane. Then the mixture was stirred for 5 min and then sonicated for 1 h, followed by grinding for 5 min. After grinding, 2 g of PDMS curing agent was added and stirred. Finally, the mixture was poured onto a polytetrafluoroethylene sheet and coated to 1 mm thickness, and further dried at 60 °C.

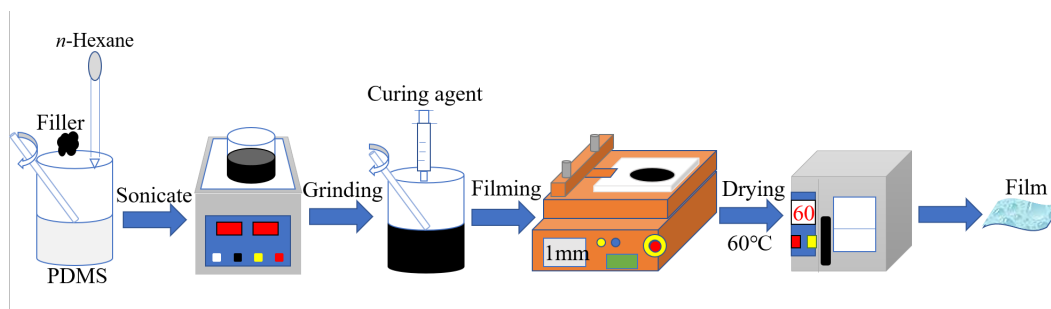


Figure 1: The fabrication process of GNP/PDMS, MGE/PDMS and BMGE/PDMS composite films.

2.4. Characterization

XRD analysis of samples using an X-ray diffractometer (XRD, D8 Advance, Bruker, Germany). The measurement range is 5° - 90° and the scanning speed is $2^{\circ}/\text{min}$. Raman tests were performed on samples using a Raman spectrometer (Raman, InVia, Renishaw, United Kingdom) and 633 nm laser excitation in the spectral range 100 cm^{-1} - 4000 cm^{-1} . The samples were ground with potassium bromide, pressed, and scanned using a Fourier transform infrared spectrometer (FTIR, Nicolet iS10, Thermo Scientific, America), with a resolution of 4 cm^{-1} , and the scanning spectral ranging from 4000 cm^{-1} to 500 cm^{-1} . The samples were placed in the crucible for TGA analysis using a thermogravimetric analyzer (TGA, STA 449 F5 Jupiter, NETZSCH, Germany).

The thickness of graphene sheets was measured by atomic force microscopy (AFM, Dimension ICON, Bruker, Germany), and the morphology of graphene nanosheets was observed. The graphene was suspended in 0.0005 wt% acetone, sonicated below 30°C for 30 min, and then the solution was dropped onto mica plates to dry. The composite films were treated with gold spray, and the cross-sectional morphologies of the films were observed using a field emission scanning electron microscope (SEM, Sigma 300, Zeiss, Germany) at an accelerating voltage of 15 kV.

Film conductivity was measured using an insulation resistance meter (6517B, Keithley, America), with a measuring range of $1\ \Omega$ - $10^{18}\ \Omega$. The electrical conductivity of graphene fillers and films with

less resistance were measured using a film thermoelectric parameter testing system (MRS-3RT, Wuhan Jiayitong Technology Co., Ltd., China).

The tensile testing machine (GX-SF001, Gongxiangyiqi, Shenzhen, China) and tensile sensor (BSA-50MT2, Transcell, America) were used to test the mechanical properties of the film, with the tensile speed of 2 mm/min. The Young's modulus and elongation at break were calculated according to the measured stress and strain data.

FLUKE data collector (2638A, Junhaizhongyi Technology, Shenzhen, China) was applied to record the resistance of the film during stretching, with the tensile machine to record the strain. The OriginLab software was applied in this study to linearly fit the strain-resistance change rate curves, and the slope of the fitted line is the Gauge Factor (GF) of the film.

3. Results and discussion

3.1. Characterization of Graphene nanoplatelets, Modified graphene and Ball-milled modified graphene

Figure 2(a) shows the XRD spectra of graphene before and after treatment, and all samples showed a diffraction peak at $2\theta = 26.5^\circ$, which is the characteristic peak of the graphite (002) crystal plane.^{18,40} Compared with the expanded GIC, the diffraction peak intensity of GNP slightly decreased, and the diffraction peak intensity of BGE-15 h and MGE decreased significantly after ball milling, indicating that the lamellae of graphene were opened, the sheet spacing increased, and the crystal integrity decreased. The diffraction peaks of BGE-9 h and BMGE are more intense, which is due to the fact that they are direct ball milling of graphene powder and short ball milling time, and less graphene lamellae are opened. Figure 2(b) shows the Raman spectra of the graphene samples with one peak each at around 1340 cm^{-1} , 1580 cm^{-1} and 2710 cm^{-1} for all samples, corresponding to the D, G and

2D peaks, respectively. The D peak corresponds to the defective and disordered structure of graphene, and the higher intensity of the D peak indicates that the more carbon atoms are hybridized by SP^3 and the more defects, I_D/I_G is usually used to indicate the degree of defects in graphene. The D peak intensity of GNP is very small, and the I_D/I_G is 0.09, indicating a high content of SP^2 ordered carbon atoms on GNP, which has a good degree of order. The intensity of the D peaks of BGE-15 h and MGE is significantly enhanced, and their defects and disordered carbon content increase after expansion and mechanical energy input in ball milling. The structurally intact graphite powder was ball milled to obtain BGE-9h and BMGE. With the increase of ball milling time, the D peak intensity of BMGE was higher than that of BGE-9 h, and the ball milling process increased the defects of graphene.⁴¹

Figure 2(c) is the FT-IR spectra of BGE-15 h and MGE. As shown in the infrared spectrum of BGE-b, a broad peak caused by -OH stretching vibration can be observed near 3441 cm^{-1} . C=O stretching vibration peaks and C=C bending vibration peaks appear at 1769 cm^{-1} and 1678 cm^{-1} , respectively. The absorption peaks appearing at 1392 cm^{-1} and 1077 cm^{-1} can be attributed to the stretching vibration of C-O-C and the bending vibration of C-OH,^{42,43} indicating that BGE-15h is rich in oxygen-containing hydrophilic groups and adsorbed water. APTES can be hydrolyzed into silanol and condensed with active hydroxyl groups on the surface of graphene, reducing the force between graphene sheets and improving its performance. Compared with BGE-15 h, the infrared spectrum of MGE changes significantly. Firstly, the stretching vibration peak corresponding to -CH₃ on APTES appeared at 2916 cm^{-1} . Due to the reaction of silanol generated by APTES hydrolysis with hydroxyl groups, the C-OH bending vibration peak disappeared, and the Si-O-C stretching vibration peak appeared at 1119 cm^{-1} , Si-O-Si stretching vibration peak appeared at 1041 cm^{-1} , which was formed by the hydrolysis and condensation of the silicon base.^{44,45} At the same time, a new absorption peak

appeared at 915 cm^{-1} , corresponding to Si-O. The absorption peaks of -OH and C=C remained in the MGE spectrum, and the hydroxyl peak became weaker, and its position had shifted to 3439 cm^{-1} . These changes in the infrared spectrum can indicate that APTES had been grafted onto BGE-15 h. Figure 2(d) is the FT-IR spectra of BGE-9 h and BMGE. After modification with APTES, it can be seen that the -OH stretching vibration peak at 3449 cm^{-1} is obviously weaker, and C=C is preserved. The stretching vibration peak of -CH₃ appeared at 2884 cm^{-1} , the bending vibration peak of C-OH disappeared, and the Si-O-C stretching vibration peak appeared at 1126 cm^{-1} . New absorption peaks appeared at 1053 cm^{-1} and 909 cm^{-1} , corresponding to Si-O-Si and Si-O.

Figure 2(e) and Figure 2(f) show the TGA curves of BGE-15 h, MGE, BGE-9 h and BMGE. After APTES modification, the thermal properties of graphene were significantly improved. When the temperature is lower than $100\text{ }^{\circ}\text{C}$, they all have a certain loss of adsorbed water mass, while BGE-15 h and BGE-9 h have more adsorbed water. When around $140\text{ }^{\circ}\text{C}$, there is a small mass loss of MGE and BMGE, which is the decomposition of APTES grafted on the surface of MGE and BMGE. The mass of BGE-15 h and BGE-9 h decreased sharply around $200\text{ }^{\circ}\text{C}$, which is due to the decomposition of the oxygen-containing functional groups on their surfaces. At higher temperatures, the chemical bonds of MGE and BMGE were broken and the carbon skeleton structures on the graphene sheets kept burning.

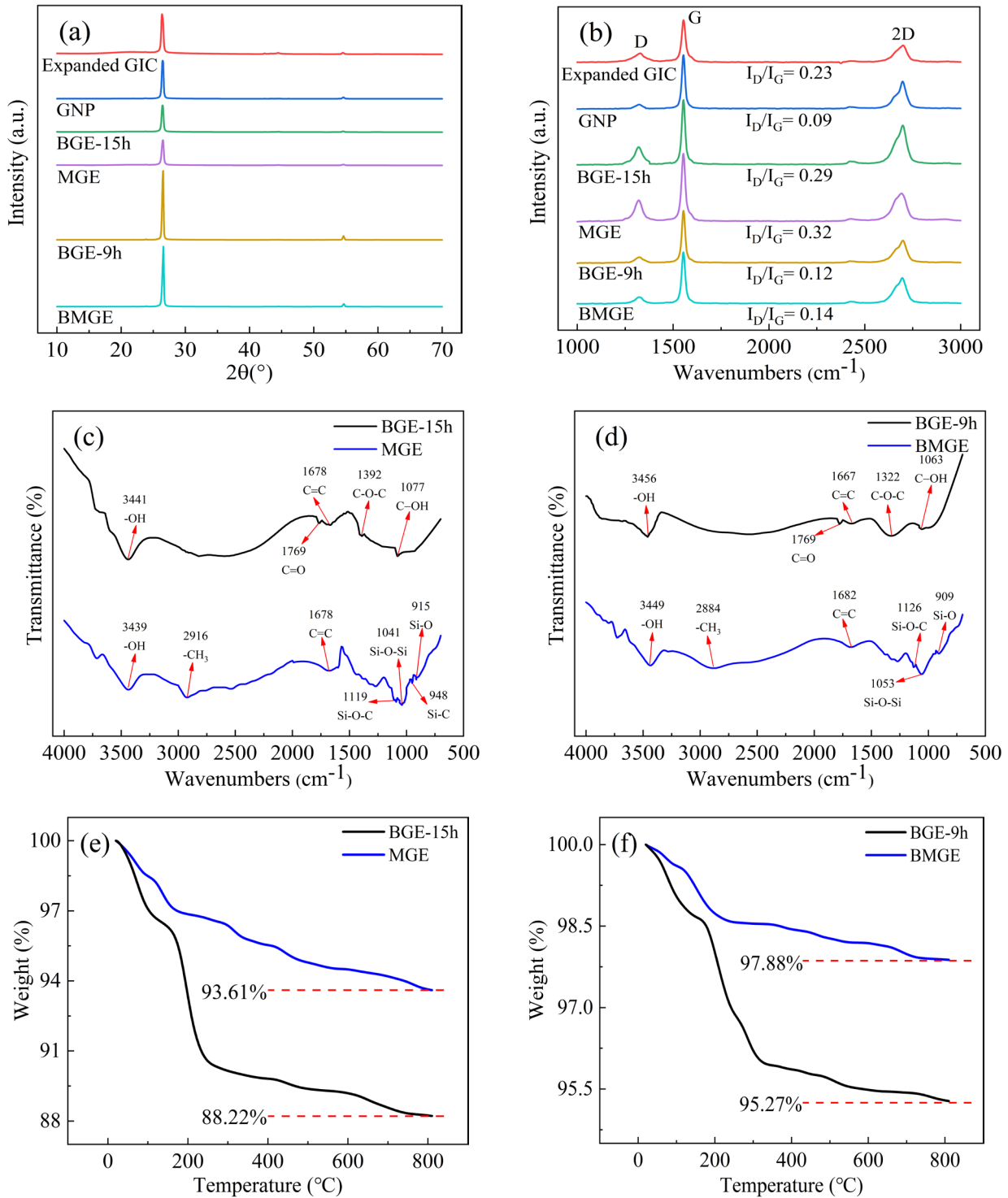


Figure 2: (a) XRD and (b) Raman analysis of expanded GIC, GNP, BGE-15 h, MGE, BGE-9 h and BMGE. (c) FT-IR spectra of BGE-15 h and MGE. (d) FT-IR spectra of BGE-9 h and BMGE. (e) TGA curves of BGE-15 h and MGE. (f) TGA curves of BGE-9 h and BMGE.

Figure 3(a) shows that GNP has a large specific surface area with a sheet layer size of about 600 nm, and the sheet edges have no distinctive features. As shown in Figure 3(d), the average thickness of GNP is 3.86 ± 0.12 nm. The thickness of the nanofiller plays an important role in the electrical

conductivity of the composites, and a lower thickness means that more graphene sheets are dispersed in the composites, forming more conductive paths. Figure 3(b) and Figure 3(e) show that the size of MGE is smaller than that of GNP, and the surface morphology does not change significantly. The average thickness of MGE was 1.71 ± 0.17 nm. During the process of ball milling, the mechanical energy input causes the weakly bonded graphene lamellae phase to peel off and the lamellae become thinner. Since ethanol and air contain oxygen-containing functional groups such as hydroxyl groups, the oxygen-containing functional groups will inevitably be attached to graphene after ball milling. As shown in Figure 3(c) and Figure 3(f), the size of BMGE is larger, with an average thickness of 4.91 ± 0.11 nm. This indicates that the graphite powder has been exfoliated and the lamellae have been reduced during the process of ball milling to obtain graphene nanomaterials. During ball milling process, the graphene edge defects were increased in the presence of shear and friction forces, and oxygen-containing functional groups were introduced in the presence of ethanol and air.

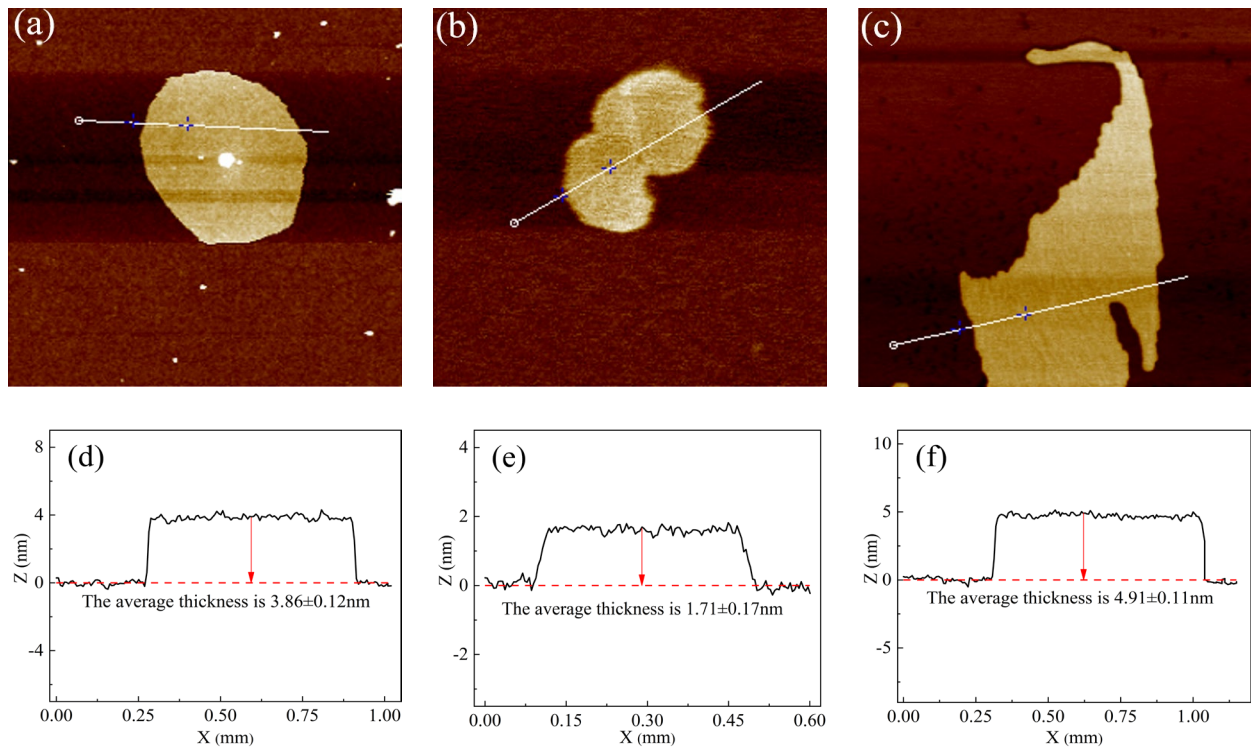


Figure 3: AFM diagram: (a) GNP, (b) MGE, and (c) BMGE. Average thickness measurement: (d) GNP, (e)

MGE, and (f) BMGE.

3.2. Mechanical property

The flexibility, tensile and compressive properties of the composite films are advantages in practical applications.⁴⁶ In Figure 4(a), the elongation at break of GNP/PDMS and MGE/PDMS composite films decreased with the increase of filler. Due to the addition of filler, the elasticity of composite films decreases, making them easier to break under tension. For example, at a filler volume fraction of 3.8%, the elongation at break of GNP/PDMS composite film and MGE/PDMS composite film are 45.7% and 50.3%, respectively, which are 28.5% and 23.9% lower than that of film without filler. This difference is mainly due to (i) the fact that GNP is poorly dispersed in PDMS and is prone to agglomeration, resulting in the composite film being highly susceptible to premature fracture at the agglomeration during loading, which affects the performance. MGE can be more uniformly dispersed in the matrix and the composite film is less likely to break during loading; (ii) APTES modification enhanced the binding between MGE and PDMS.^{29,47} And the elongation at break of BMGE/PDMS composite film increases and then decreases, which is much higher than that of GNP/PDMS composite film and MGE/PDMS composite film. At 1.9 vol%, the elongation at break of BMGE/PDMS composite film is 93.8%. This may be because BMGE is prepared from graphite powder, which retains some properties of graphite powder, such as high surface activity, lubricity and adsorption. After APTES modification, the interfacial bond with PDMS is stronger and tighter. As shown in Figure 4(b), the Young's modulus of the three composite films increases with the fillers. The Young's modulus of MGE/PDMS composite film is slightly lower than that of GNP/PDMS composite film, and the Young's modulus of BMGE/PDMS composite film is higher than that of MGE/PDMS and GNP/PDMS composite films. In Figure 4(c), with the increase of filler, the tensile

strengths of the three composite films first increased and then decreased. After adding a small amount of fillers, the rigidity of the composite film increased and was not easily deformed, which increased the tensile strength of the composite film. When there are more fillers, the agglomeration of nanoparticles or the accumulation of nanosheets tends to reduce the tensile strength, and the composite film is more likely to break during the stretching process. The tensile strength of the BMGE/PDMS composite film is the highest.

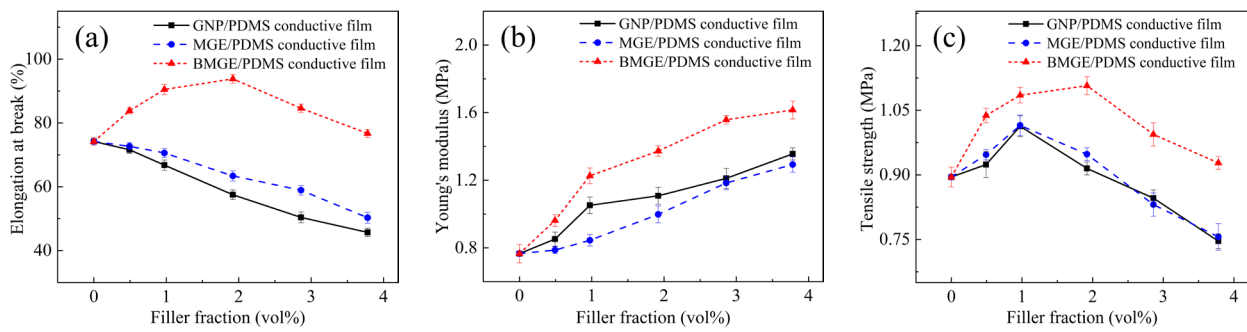


Figure 4: (a) Elongation at break, (b) Young's modulus and (c) tensile strength of GNP/PDMS, MGE/PDMS and BMGE/PDMS composite films.

3.3. Electrical conductivity

According to the theory of particle-filled composite conductive percolation threshold,^{48,49} when the volume fraction of conductive particles is small, the conductive particles are discrete from each other, the conductivity of the composite material is very low. When the volume fraction of conductive particles increases to a certain threshold value, the conductivity of the composite material suddenly increases, and the change can reach more than 10 orders of magnitude. Then with the increase of volume fraction of conductive particles, the conductivity of the composite material decreases slowly, and the corresponding threshold of the volume fraction of conductive particles is called percolation threshold, The equation for the percolation threshold is:

$$\sigma_c = \sigma_f (\varphi - \varphi_t)^t \quad (1)$$

Where σ_c is the conductivity of the composites, σ_f is the conductivity of the filled particles, ϕ is the volume fraction of filled particles, ϕ_t is the permeability threshold of composites, and t is the critical exponent.^{16,50} The addition of fillers greatly improves the electrical conductivity of the composites, so we need to find the percolation thresholds of the three composite films. The conductivities of GNP, MGE and BMG were measured to be 1881.88 S/cm, 1317.86 S/cm, and 780.71 S/cm, respectively.

Figure 5 shows the electrical conductivities of GNP/PDMS, MGE/PDMS and BMGE/PDMS composite films. When the volume fraction of filler is less than 1.5%, the electrical conductivity of the three composite films is very low, because there is no or little contact between the graphene sheet layers, and no conductive network is formed. When the volume fraction of filler is greater than 1.5%, the conductive network is gradually formed, and the conductivity starts to increase, and the conductivity increases sharply at 1.5 vol% - 2.8 vol%. When the volume fraction of filler is greater than 2.8%, the conductivity grows slowly. Bringing the data into Equation 1, their percolation thresholds were calculated to be 2.27 vol%, 2.31 vol% and 2.66 vol%, respectively. Based on the above discussion, 3vol% composite films will be selected as a representative study target in the following studies.

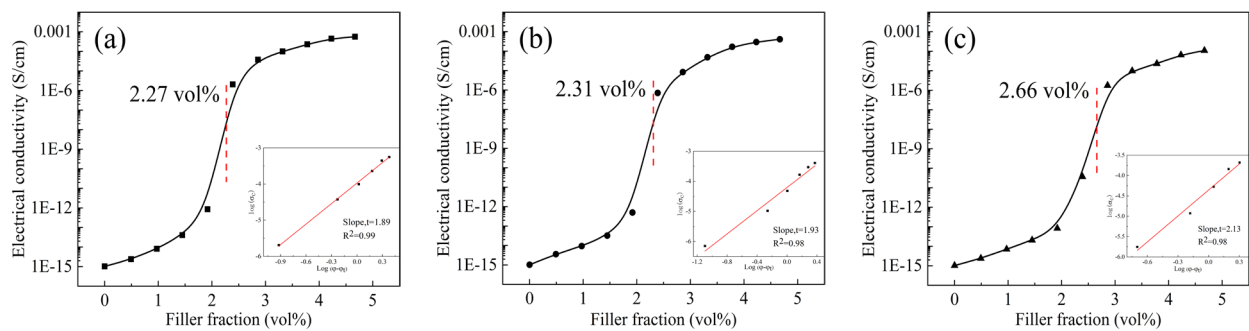


Figure 5: The electrical conductivity of (a) GNP/PDMS, (b) MGE/PDMS and (c) BMGE/PDMS composite films.

3.4. Film morphology analysis

As shown in Figure 6(a1, a2, a3), the GNPs are stacked together and wrapped by the PDMS matrix to form a wrinkled structure, and the GNPs are connected to each other to form a conductive network, which makes the composite film with good conductivity. However, the dispersion of GNPs in PDMS is not uniform, and the region indicated by the yellow arrow in Figure 6(a1) is relatively flat, indicating that there are few GNPs in this area. In other regions, more GNPs are clustered together, which affects the electrical conductivity and mechanical properties of the films. In addition, there are many voids in the cross section of GNP/PDMS composite films, as shown by the yellow arrows in Figure 6(a2, a3).

Figure 6(b1, b2, b3) show the cross-sectional morphology of the MGE/PDMS composite films. Compared with GNP, MGE is relatively uniformly dispersed in PDMS, and folded structures exist in all regions of the cross section with similar amounts. There are fewer gaps in the cross-section of MGE/PDMS composite films, indicating that the binding effect of MGE is better than GNP'. Due to the smaller thickness of MGE, there will be more graphene sheets dispersed in PDMS, resulting in a more uniform distribution and forming more conductive paths. As shown in Figure 6(c1, c2, c3), the BMGE/PDMS composite film has less wrinkled structures compared to the MGE/PDMS composite film. Since the sheet of BMGE are thicker, fewer sheets are dispersed in the PDMS, thus forming fewer conductive paths. In addition, it can be seen that there are more gaps in the cross-section of the BMGE/PDMS composite film than the MGE/PDMS composite film.

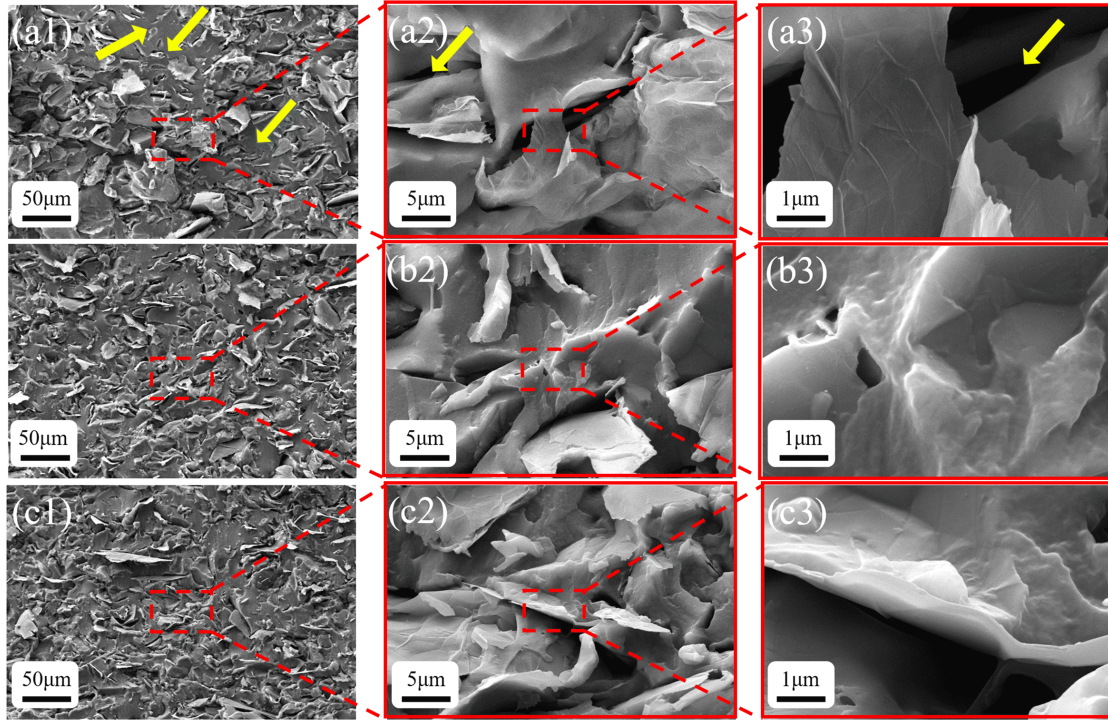


Figure 6: The SEM images of (a1, a2, a3) GNP/PDMS, (b1, b2, b3) MGE/PDMS and (c1, c2, c3) BMGE/PDMS composite films.

3.5. Sensing performance

Sensitivity is the one of the most important properties of a sensor. The sensitivity of a strain sensor is expressed as a gauge factor (GF), calculated as:

$$GF = \frac{\Delta R/R_0}{\Delta L/L_0} = \frac{\Delta R/R_0}{\varepsilon} \quad (2)$$

where ΔR is the resistance variation value during stretching, R_0 is the initial resistance of the composite film, ΔL is the elongation of the composite film, and L_0 is the initial length of the composite film.^{51,52} Linearity refers to the degree to which the sensor strain and output resistance curves do not agree with the fitted straight line. R^2 of the fitted straight line is the linearity of the sensor, and if the linearity of the sensor is higher in a certain strain range, the calculation of sensitivity within the range is more accurate. The test was performed by fixing the both ends of the composite film with a tensile machine jig, using a sandpaper to prevent damage to the composite film when the

jig was clamped. The tensile speed was kept constant and the resistance data and strain data were recorded continuously.

In Figure 7(a) and Figure 7(b), the sensing ranges of GNP/PDMS composite film and MGE/PDMS composite film are 40% and 48%, respectively. According to the calculations, the GFs of MGE/PDMS composite films are 46 and 57 in the 0%-20% strain range, 141 and 152 in the 20%-40% strain range, and 156 in the 40%-48% strain range, respectively. The sensing range and sensitivity of the MGE/PDMS composite film are higher than those of GNP/PDMS composite film. Due to the ball milling treatment and APTES modification, the thickness and size of MGE are smaller, and more sheets can be dispersed in the matrix with uniform dispersion, creating more conductive paths within the matrix. Moreover, the contact area between MGE sheets is smaller, and the sheets separate from each other after being subjected to external forces, resulting in larger resistance changes. As shown in Figure 7(c), the sensing range of the BMGE/PDMS composite film is 57%, which is the largest comparing to the other two composite films. The GF is 40 at 0%-20% strain, 137 at 20%-40% strain, and 146 at 40%-57% strain. BMGE/PDMS composite film shows less sensitivity and still cannot meet the sensitivity requirements of many flexible devices. The larger thickness and size of BMGE results in fewer sheets in the substrate, resulting in fewer conductive paths. Although the larger contact area between BMGE sheets allows for a larger sensing range, the smaller change in resistance at under load will affect sensitivity.

Figure 7(d) shows the resistances of the three composite films at different bending angles. The composite films have good flexibility, can be restored to its original shape without cracks after being bent to 180°. The initial resistance of all the composite films is around 15 k Ω , and the resistance of the composite films increases with the bending angles. The resistance change of MGE/PDMS

composite film is the largest, and the resistance change of BMGE/PDMS composite film is the smallest, which is consistent with the analysis of sensitivity. This shows the potential of composite films in monitoring bending deformation.

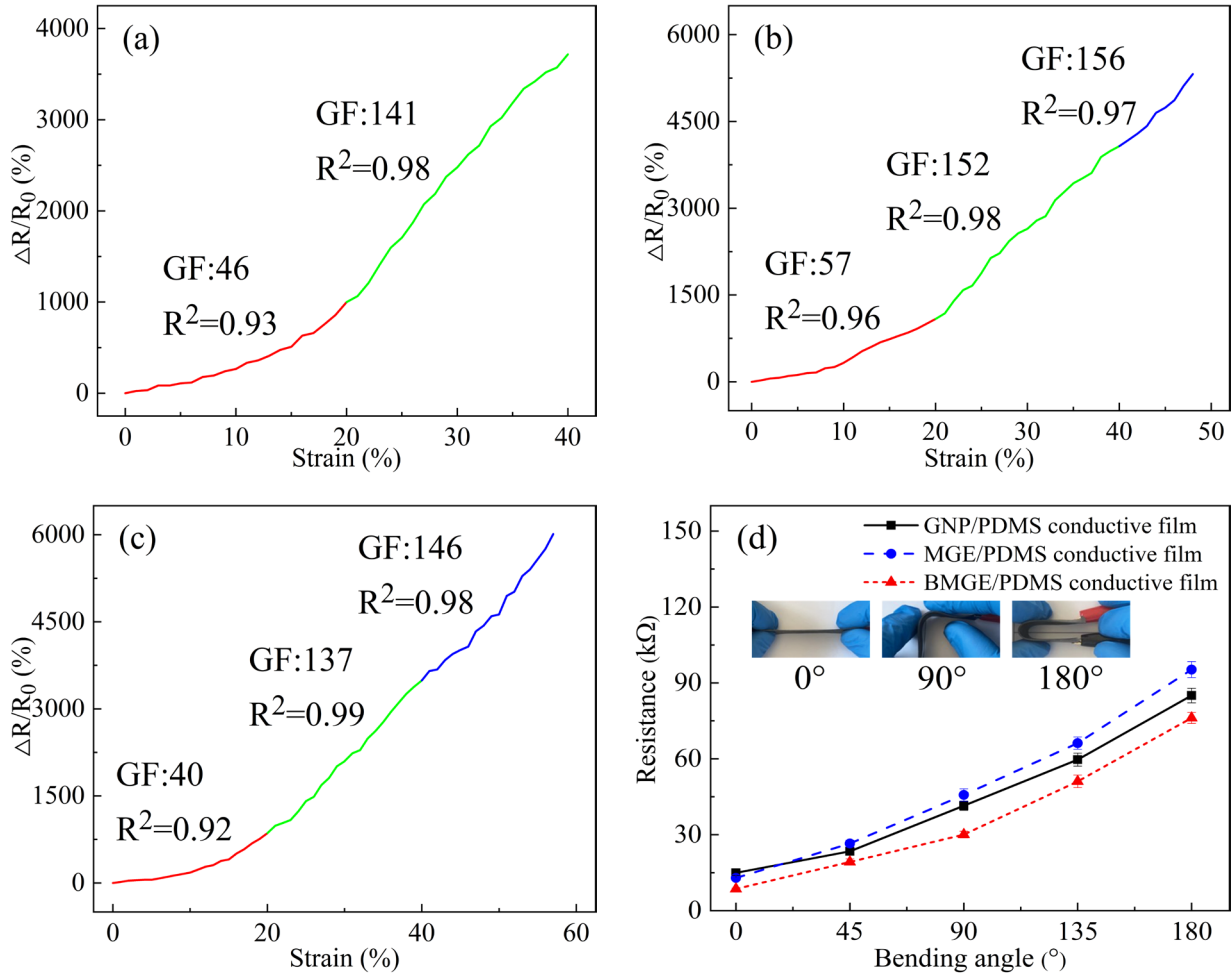


Figure 7: The relative resistance variation versus tensile strain curves of (a) GNP/PDMS, (b) MGE/PDMS and (c) BMGE/PDMS composite films. (d) The resistive responses to bending deformation of GNP/PDMS, MGE/PDMS and BMGE/PDMS composite films.

The response time is the reaction time for the sensor to undergo a corresponding change in resistance after being stretched. As shown in Figure 8(a, b, c), the resistance of the composite film does not reach its maximum value at the same time after the strain reached 15%, but reaches its maximum value after a certain period of time. The resistance change of GNP/PDMS composite film is about 5 times, the resistance change of MGE/PDMS composite film is about 7.5 times, and the resistance change of BMGE/PDMS composite film is about 4 times. Their response times are 0.15 s, 0.12 s and

0.12 s, respectively.

To test the response of the composite film to small strains, the tensile deformation experienced by the film was gradually increased from 0.1% to 0.5%. In Figure 8(d), the resistance of the composite film increases with increasing strain, and the MGE/PDMS composite film has the largest change in resistance. For example, when the strain increases to 0.5%, the change in resistances of GNP/PDMS, MGE/PDMS, and BMGE/PDMS composite films are about 0.04 times, 0.06 times and 0.045 times, respectively, indicating that the composite films can detect small strains.

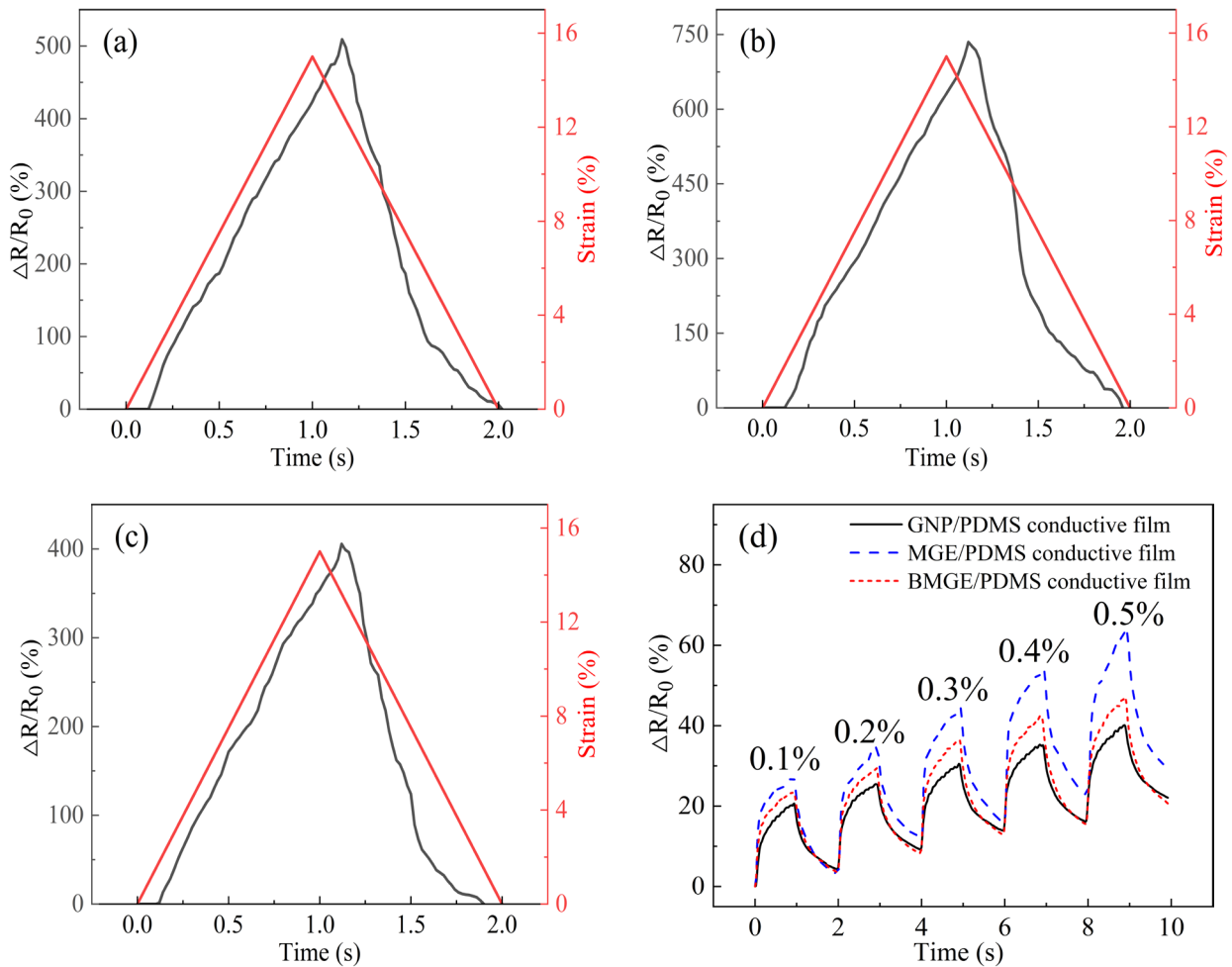


Figure 8: The response time of (a) GNP/PDMS, (b) MGE/PDMS and (c) BMGE/PDMS composite films. (d) The relative resistance variation step tensile strains of GNP/PDMS, MGE/PDMS and BMGE/PDMS composite films.

To investigate the stability and repeatability of the composite films, 10,000 cyclic load-unload tests on three composite films with a strain of 2% were performed. As shown in Figure 9(a, b, c), their

change in resistances is very stable with only a small range of variation. In the enlarged plots of the first 100 cycles and the last 100 cycles of the GNP/PDMS composite films, it can be seen that the middle value of the resistance variation range drops from -5 to -10, which is caused by the change in the initial structure of the graphene interior and interface.⁵³ Compared to the GNP/PDMS composite films, the MGE/PDMS and BMGE/PDMS composite films are more stable, and their resistance change ranges remain almost constant after 3000 cycles. This indicates that the composite films have long-term stability and repeatability.

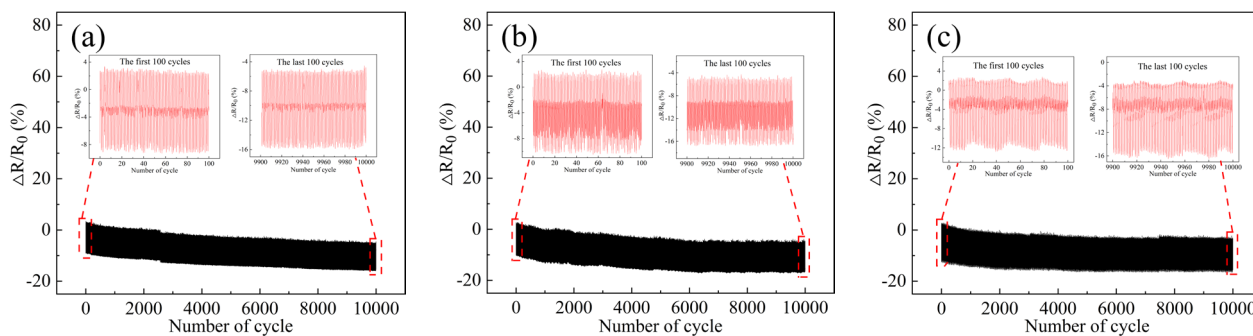


Figure 9: The relative resistance variation under 10000 stretching-releasing cycles at the strain of 2% of (a) GNP/PDMS, (b) MGE/PDMS and (c) BMGE/PDMS composite films.

4. Conclusion

In this work, three graphene fillers were prepared by thermal expansion-ultrasonication, thermal expansion-ball milling-APTES modified and ball milling-APTES modified graphene powders, and the effects of the addition of the three fillers on the electrical and mechanical properties of the composite films were further investigated. The results showed that the electrical and mechanical properties of the films were related to the filler properties, the thickness and size of the sheets, and the degree of dispersion in the PDMS matrix. Compared with GNP/PDMS composite films, the mechanical properties and electrical conductivity of MGE/PDMS composite film are improved. BMGE/PDMS composite film shows the best result of mechanical properties comparing to the other

two composite films, but its sensitivity is the lowest. Due to the different raw materials used in the preparation of fillers, BMGE is more suitable for enhancing the mechanical performance of PDMS. The excellent sensing performance of MGE/PDMS composite films demonstrate its great potential in various future practical applications, such as human motion monitoring, personal healthcare and structural monitoring.

Reference

1. Tang J, Wu Y, Ma S, Yan T, Pan Z. Flexible strain sensor based on CNT/TPU composite nanofiber yarn for smart sports bandage. *Composites Part B: Engineering*. 2022;232:109605.
2. Kim DH, Lu N, Ma R, et al. Epidermal electronics. *Science*. Aug 12 2011;333(6044):838-43. doi:10.1126/science.1206157
3. Hammock ML, Chortos A, Tee BC, Tok JB, Bao Z. 25th anniversary article: The evolution of electronic skin (e-skin): a brief history, design considerations, and recent progress. *Adv Mater*. Nov 13 2013;25(42):5997-6038. doi:10.1002/adma.201302240
4. Honda W, Harada S, Arie T, Akita S, Takei K. Wearable, Human-Interactive, Health-Monitoring, Wireless Devices Fabricated by Macroscale Printing Techniques. *Advanced Functional Materials*. 2014;24(22):3299-3304. doi:10.1002/adfm.201303874
5. Wang Y, Wang Y, Yang Y. Graphene-Polymer Nanocomposite-Based Redox-Induced Electricity for Flexible Self-Powered Strain Sensors. *Advanced Energy Materials*. 2018;8(22)doi:10.1002/aenm.201800961
6. Han S, Zhang X, Wang P, et al. Mechanically robust, highly sensitive and superior cycling performance nanocomposite strain sensors using 3-nm thick graphene platelets. *Polymer Testing*. 2021;98doi:10.1016/j.polymertesting.2021.107178
7. Zhou Y, Stewart R. Highly flexible, durable, UV resistant, and electrically conductive graphene based TPU/textile composite sensor. *Polymers for Advanced Technologies*. 2022;33(12):4250-4264.
8. Sun H, Dai K, Zhai W, et al. A Highly Sensitive and Stretchable Yarn Strain Sensor for Human Motion Tracking Utilizing a Wrinkle-Assisted Crack Structure. *ACS Appl Mater Interfaces*. Oct 2 2019;11(39):36052-36062. doi:10.1021/acsami.9b09229
9. Yin J, Lu C, Li C, et al. A UV-filtering, environmentally stable, healable and recyclable ionic hydrogel towards multifunctional flexible strain sensor. *Composites Part B: Engineering*. 2022;230:109528.
10. Sun R, Gao L, Liu F, et al. Magnetically induced robust anisotropic structure of multi-walled carbon nanotubes/Ni for high-performance flexible strain sensor. *Carbon*. 2022;194:185-196.
11. Pan F, Chen S-M, Li Y, et al. 3D Graphene Films Enable Simultaneously High Sensitivity and Large Stretchability for Strain Sensors. *Advanced Functional Materials*. 2018;28(40)doi:10.1002/adfm.201803221
12. Shi X, Liu S, Sun Y, Liang J, Chen Y. Lowering Internal Friction of 0D-1D-2D Ternary Nanocomposite-Based Strain Sensor by Fullerene to Boost the Sensing Performance. *Advanced*

Functional Materials. 2018;28(22)doi:10.1002/adfm.201800850

13. Chen Y-F, Huang M-L, Cai J-H, Weng Y-X, Wang M. Piezoresistive anisotropy in conductive silicon rubber/multi-walled carbon nanotube/nickel particle composites via alignment of nickel particles. *Composites Science and Technology*. 2022:109520.
14. Cai J-H, Li J, Chen X-D, Wang M. Multifunctional polydimethylsiloxane foam with multi-walled carbon nanotube and thermo-expandable microsphere for temperature sensing, microwave shielding and piezoresistive sensor. *Chemical Engineering Journal*. 2020;393doi:10.1016/j.cej.2020.124805
15. Meng Q, Yu Y, Tian J, et al. Multifunctional, durable and highly conductive graphene/sponge nanocomposites. *Nanotechnology*. Nov 13 2020;31(46):465502. doi:10.1088/1361-6528/ab9f73
16. Han S, Chand A, Araby S, et al. Thermally and electrically conductive multifunctional sensor based on epoxy/graphene composite. *Nanotechnology*. Feb 7 2020;31(7):075702. doi:10.1088/1361-6528/ab5042
17. Ioniță M, Vlăsceanu GM, Watzlawek AA, Voicu SI, Burns JS, Iovu H. Graphene and functionalized graphene: Extraordinary prospects for nanobiocomposite materials. *Composites Part B: Engineering*. 2017;121:34-57. doi:10.1016/j.compositesb.2017.03.031
18. Yang Y, Tao J-R, Yang D, He Q-M, Chen X-D, Wang M. Improving dispersion and delamination of graphite in biodegradable starch materials via constructing cation- π interaction: Towards microwave shielding enhancement. *Journal of Materials Science & Technology*. 2022;
19. Wu Z, Jiang X, Li Y, et al. Microstructures and properties of graphene nanoplatelets reinforced Cu/Ti₃SiC₂/C nanocomposites with efficient dispersion and strengthening achieved by high-pressure torsion. *Materials Characterization*. 2022;193:112308.
20. Cha J, Kim J, Ryu S, Hong SH. Comparison to mechanical properties of epoxy nanocomposites reinforced by functionalized carbon nanotubes and graphene nanoplatelets. *Composites Part B: Engineering*. 2019;162:283-288. doi:10.1016/j.compositesb.2018.11.011
21. Zhou Y, Myant C, Stewart R. Multifunctional and stretchable graphene/textile composite sensor for human motion monitoring. *Journal of Applied Polymer Science*. 2022;139(32):e52755.
22. Zhang C, Li W, Liu C, et al. Effect of covalent organic framework modified graphene oxide on anticorrosion and self-healing properties of epoxy resin coatings. *Journal of Colloid and Interface Science*. 2022;608:1025-1039.
23. Villalonga A, Estabiel I, Pérez-Calabuig AM, Mayol B, Parrado C, Villalonga R. Amperometric aptasensor with sandwich-type architecture for troponin I based on carboxyethylsilanetriol-modified graphene oxide coated electrodes. *Biosensors and Bioelectronics*. 2021;183:113203.
24. Chua CK, Pumera M. Covalent chemistry on graphene. *Chem Soc Rev*. Apr 21 2013;42(8):3222-33. doi:10.1039/c2cs35474h
25. Li H, Qiang Y, Zhao W, Zhang S. 2-Mercaptobenzimidazole-inbuilt metal-organic-frameworks modified graphene oxide towards intelligent and excellent anti-corrosion coating. *Corrosion Science*. 2021;191:109715.
26. Ding J-H, Zhao H-R, Zheng Y, Zhao X, Yu H-B. A long-term anticorrosive coating through graphene passivation. *Carbon*. 2018;138:197-206. doi:10.1016/j.carbon.2018.06.018
27. Mateos-Gil J, Rodríguez-Pérez L, Moreno Oliva M, et al. Electroactive carbon nanoforms: a comparative study via sequential arylation and click chemistry reactions. *Nanoscale*. 2015;7(3):1193-1200. doi:10.1039/c4nr04365k
28. Alam A, Wan C, McNally T. Surface amination of carbon nanoparticles for modification of

- epoxy resins: plasma-treatment vs. wet-chemistry approach. *European Polymer Journal*. 2017;87:422-448. doi:10.1016/j.eurpolymj.2016.10.004
29. Xu H, Gong L-X, Wang X, et al. Influence of processing conditions on dispersion, electrical and mechanical properties of graphene-filled-silicone rubber composites. *Composites Part A: Applied Science and Manufacturing*. 2016;91:53-64. doi:10.1016/j.compositesa.2016.09.011
 30. Tang L-C, Wan Y-J, Yan D, et al. The effect of graphene dispersion on the mechanical properties of graphene/epoxy composites. *Carbon*. 2013;60:16-27. doi:10.1016/j.carbon.2013.03.050
 31. Mateti S, Mathesh M, Liu Z, et al. Mechanochemistry: A force in disguise and conditional effects towards chemical reactions. *Chem Commun (Camb)*. Feb 2 2021;57(9):1080-1092. doi:10.1039/d0cc06581a
 32. Zhao W, Fang M, Wu F, Wu H, Wang L, Chen G. Preparation of graphene by exfoliation of graphite using wet ball milling. *Journal of Materials Chemistry*. 2010;20(28)doi:10.1039/c0jm01354d
 33. Pourhashem S, Vaezi MR, Rashidi A, Bagherzadeh MR. Distinctive roles of silane coupling agents on the corrosion inhibition performance of graphene oxide in epoxy coatings. *Progress in Organic Coatings*. 2017;111:47-56. doi:10.1016/j.porgcoat.2017.05.008
 34. Li W, Zhou B, Wang M, Li Z, Ren R. Silane functionalization of graphene oxide and its use as a reinforcement in bismaleimide composites. *Journal of Materials Science*. 2015;50(16):5402-5410. doi:10.1007/s10853-015-9084-z
 35. Wan Y-J, Gong L-X, Tang L-C, Wu L-B, Jiang J-X. Mechanical properties of epoxy composites filled with silane-functionalized graphene oxide. *Composites Part A: Applied Science and Manufacturing*. 2014;64:79-89. doi:10.1016/j.compositesa.2014.04.023
 36. Wang X, Xing W, Zhang P, Song L, Yang H, Hu Y. Covalent functionalization of graphene with organosilane and its use as a reinforcement in epoxy composites. *Composites Science and Technology*. 2012;72(6):737-743. doi:10.1016/j.compscitech.2012.01.027
 37. Woraphutthaporn S, Pattananuwat P, Hayichelaeh C, Kobayashi T, Boonkerd K. Enhancing the properties of graphene oxide/natural rubber nanocomposite - based strain sensor modified by amino - functionalized silanes. *Polymers for Advanced Technologies*. 2022;
 38. Lotfi M, Yari H, Sari MG, Azizi A. Fabrication of a highly hard yet tough epoxy nanocomposite coating by incorporating graphene oxide nanosheets dually modified with amino silane coupling agent and hyperbranched polyester-amide. *Progress in Organic Coatings*. 2022;162:106570.
 39. Meng Q, Kuan H-C, Araby S, et al. Effect of interface modification on PMMA/graphene nanocomposites. *Journal of Materials Science*. 2014;49(17):5838-5849. doi:10.1007/s10853-014-8278-0
 40. Jeon IY, Shin YR, Sohn GJ, et al. Edge-carboxylated graphene nanosheets via ball milling. *Proc Natl Acad Sci U S A*. Apr 10 2012;109(15):5588-93. doi:10.1073/pnas.1116897109
 41. Xu J, Zhao X, Liu F, Jin L, Chen G. Preparation of graphene via wet ball milling and in situ reversible modification with the Diels–Alder reaction. *New Journal of Chemistry*. 2020;44(4):1236-1244. doi:10.1039/c9nj05309c
 42. Mao M, Yu K-X, Cao C-F, et al. Facile and green fabrication of flame-retardant Ti3C2Tx MXene networks for ultrafast, reusable and weather-resistant fire warning. *Chemical Engineering Journal*. 2022;427:131615.
 43. Guo K-Y, Wu Q, Mao M, et al. Water-based hybrid coatings toward mechanically flexible, super-hydrophobic and flame-retardant polyurethane foam nanocomposites with high-efficiency and

- reliable fire alarm response. *Composites Part B: Engineering*. 2020;193doi:10.1016/j.compositesb.2020.108017
44. Zhang Z-H, Zhang J-W, Cao C-F, et al. Temperature-responsive resistance sensitivity controlled by L-ascorbic acid and silane co-functionalization in flame-retardant GO network for efficient fire early-warning response. *Chemical Engineering Journal*. 2020;386doi:10.1016/j.cej.2019.123894
 45. Wu Q, Gong LX, Li Y, et al. Efficient Flame Detection and Early Warning Sensors on Combustible Materials Using Hierarchical Graphene Oxide/Silicone Coatings. *ACS Nano*. Jan 23 2018;12(1):416-424. doi:10.1021/acsnano.7b06590
 46. Zheng Y, Li Y, Zhou Y, et al. High-Performance Wearable Strain Sensor Based on Graphene/Cotton Fabric with High Durability and Low Detection Limit. *ACS Appl Mater Interfaces*. Jan 8 2020;12(1):1474-1485. doi:10.1021/acsaami.9b17173
 47. Li Y-T, Liu W-J, Shen F-X, et al. Processing, thermal conductivity and flame retardant properties of silicone rubber filled with different geometries of thermally conductive fillers: A comparative study. *Composites Part B: Engineering*. 2022;238:109907.
 48. Araby S, Meng Q, Zhang L, et al. Electrically and thermally conductive elastomer/graphene nanocomposites by solution mixing. *Polymer*. 2014;55(1):201-210. doi:10.1016/j.polymer.2013.11.032
 49. Ma J, Meng Q, Michelmore A, et al. Covalently bonded interfaces for polymer/graphene composites. *Journal of Materials Chemistry A*. 2013;1(13)doi:10.1039/c3ta01277h
 50. Han S, Meng Q, Chand A, et al. A comparative study of two graphene based elastomeric composite sensors. *Polymer Testing*. 2019;80doi:10.1016/j.polymertesting.2019.106106
 51. Li X, Hua T, Xu B. Electromechanical properties of a yarn strain sensor with graphene-sheath/polyurethane-core. *Carbon*. 2017;118:686-698. doi:10.1016/j.carbon.2017.04.002
 52. Zhang S, Zhang H, Yao G, et al. Highly stretchable, sensitive, and flexible strain sensors based on silver nanoparticles/carbon nanotubes composites. *Journal of Alloys and Compounds*. 2015;652:48-54. doi:10.1016/j.jallcom.2015.08.187
 53. He Y, Wu D, Zhou M, et al. Wearable Strain Sensors Based on a Porous Polydimethylsiloxane Hybrid with Carbon Nanotubes and Graphene. *ACS Appl Mater Interfaces*. Apr 7 2021;13(13):15572-15583. doi:10.1021/acsaami.0c22823